Applied Catalysis B: Environmental 129 (2013) 80–88

Contents lists available at SciVerse ScienceDirect

Applied Catalysis B: Environmental

journal homepage: www.elsevier.com/locate/apcatb

One-pot synthesis of In_2S_3 nanosheets/graphene composites with enhanced visible-light photocatalytic activity

Xiaoqiang An[a,b], Jimmy C. Yu[a,*], Feng Wang[a], Chuanhao Li[a], Yecheng Li[a]

[a] Department of Chemistry and Institute of Environment, Energy and Sustainability, The Chinese University of Hong Kong, Shatin, New Territories, Hong Kong, China
[b] Department of Fire Protection Engineering, Chinese People's Armed Police Academy, Langfang, Hebei 065000, PR China

ARTICLE INFO

Article history:
Received 12 June 2012
Received in revised form 30 August 2012
Accepted 9 September 2012
Available online 17 September 2012

Keywords:
Graphene
Photocatalyst
Indium sulfide

ABSTRACT

Novel In_2S_3 nanosheets/graphene photocatalysts were fabricated by a cysteine-assisted one-pot hydrothermal method. Due to the intimate interfacial contact and efficient charge separation, superior visible-light activity for degrading organic dyes and reducing Cr(VI) were achieved. During the decoloring process of methyl orange, the average apparent rate for the as-synthesized composites with 1% graphene was almost 5 times higher than that of pure In_2S_3. This work provides new insights into utilizing In_2S_3/graphene composites as high-efficiency visible-light-driven photocatalysts for environmental remediation and energy conversion.

1. Introduction

Photocatalytic nanomaterials are attracting more and more attention because of their potential for solving environmental and energy problems, which are the biggest challenges of the 21st century. Despite the remarkable advances since the emergence of photocatalytic technology, the application of the common TiO_2-based photocatalyst is significantly limited because of the recombination of electron–hole pairs and mismatch between the band gap energy and sunlight spectra [1]. Thus, numerous attempts have been made on the fabrication of semiconductor nanomaterials as potential alternative photocatalysts with desirable visible light activities [2].

Several photocatalysts with visible-light activities has been reported, including $TiO_{2-x}N_x$, CdS/graphene, Ag_3PO_4, $BiVO_4$ and Bi_2WO_6[3–6]. In_2S_3, a III–VI group sulfide with a band gap of 2.0–2.3 eV have attracted intense interest for optical, photoconductive and optoelectronic applications [7]. Due to its high photosensitivity and photoconductivity, stable chemical and physical characteristics and low toxicity, In_2S_3 shows great potential for visible-light-driven photodegradation of pollutants and photocatalytic water splitting. Many attempts have been explored to fabricate In_2S_3 nanostructures with different morphologies, such as In_2S_3 nanoplates, nanotubes, hollow microspheres and nanorods [8–10].

Graphene is a novel material, with a large theoretical specific surface area and high intrinsic electron mobility. Its optical transmittance, large surface area and high electrical conductivity are valuable in promoting electron transfer in electrochemical, photocatalytic and sensing reactions. Recently, graphene-based assemblies are gaining attention as a viable alternate route to boost the efficiency of photocatalysts [11]. To date, several graphene-based composites have been reported for their improved photocatalytic properties [12]. However, little attention has been given to In_2S_3/graphene nanocomposites.

In this work, In_2S_3 nanosheets/graphene composites were fabricated through a cysteine-assisted one-pot hydrothermal reaction. With multifunctional groups, cysteine acted as a sulfide source for the growth of In_2S_3 and as a reducing agent for the reduction of graphene oxide (GO). Due to the perfect interfacial contact and efficient charge separation, the as-synthesized composites showed superior visible light activities than that of either pure In_2S_3 nanostructures or some other visible-light-driven photocatalysts. The promising applications of In_2S_3 nanosheets/graphene composites for photodegradation of organic dyes and photocatalytic reduction of toxic Cr(VI) were well presented. This study shows a green chemical route to fabricate graphene-based photocatalysts.

2. Experimental

2.1. Synthesis of In_2S_3 nanosheets/graphene composites

Graphene oxide was synthesized from flake graphite by a modified Hummers method [13]. In_2S_3 nanosheets/graphene composites were synthesized by a one-step hydrothermal growth

* Corresponding author. Tel.: +852 3943 6268; fax: +852 2603 5057.
E-mail address: jimyu@cuhk.edu.hk (J.C. Yu).

0926-3373/$ – see front matter © 2012 Elsevier B.V. All rights reserved.
http://dx.doi.org/10.1016/j.apcatb.2012.09.008

reaction. In a typical process, 0.3 mmol $InCl_3$ and 0.9 mmol cysteine were dissolved in 30 mL of DI water. Then a specific amount of graphene oxide solution was added and kept stirring for 2 h to get a homogeneous solution. The solution was transferred into a Teflon-lined autoclave and maintained at 180 °C for 24 h. The final product was centrifuged, washed with water and dried at room temperature. Pure In_2S_3 were fabricated through a similar procedure, in the absence of GO. For comparison, series of In_2S_3/graphene photocatalysts were fabricated by changing the amount of GO, reaction temperature, the molar ratio of In^{3+} and cysteine.

2.2. Characterization

The morphology of the products was characterized by field-emission scanning electron microscope (FESEM, FEI, Quanta 400 FEG) and transmission electron microscopy (TEM, Philips, CM120). A 200 kV transmission electron microscope equipped with a Gatan Imaging Filter was used to characterize the graphene sheets by high-resolution transmission electron microscopy (HRTEM, FEI, TecnaiF20) and electron energy loss spectroscopy (EELS). X-ray diffraction (XRD) patterns were recorded using a Bruker D8 advance diffractometer with high-intensity Cu Kα1 irradiation (λ = 1.5406 Å). UV–vis spectra were recorded on a Varian Cary 500 Scan UV–visible system. The structure of composites was characterized by Micro Raman Spectrometer (Renishaw, RM-100). The XPS data were determined on an AXIS Ultra instrument (Kratos, UK).

2.3. Photoelectrochemical behavior of In_2S_3/graphene composites

Five-milligrams of composite and 10 μl of Nafion solution (5 wt%) were dispersed in a 1 ml water/isopropanol mixed solvent (3:1 v/v) by at least 30 min sonication to form a homogeneous catalyst colloid. For the photocurrent measurements, 100 μl of the catalyst colloid was deposited onto areas of ca. 1 cm^2 of the ITO glass. A platinum wire was used as a counter electrode while an Ag/AgCl electrode worked as the reference electrode. The electrolyte was a 1 M KCl solution degassed with Ar. The illumination source was a 300 W xenon lamp with a 400 nm cutoff filter. The photocurrent measurement was carried out with an electrochemical workstation system (Parstat 2273, Princeton Applied Research).

2.4. Fabrication of reference photocatalysts

The preparation of Ag_3PO_4 was the same as that described in Ref. [4]. In a typical process, 0.2 g of CH_3COOAg was dissolved in 20 mL of DI water. Then, Na_2HPO_4 aqueous solution (0.15 M) was added with drop by drop to the solution and stirred for 2 h. The yellow precipitation was washed with water and dried at room temperature. The method described in Ref. [5] was used to fabricate nitrogen doped TiO_2 (N–TiO_2). 17 mL of tetrabutylorthotitanate were added into 1 wt% $NH_3{\cdot}H_2O$ solution under stirring. The solution was stirred for 1 h and then aged at room temperature. Finally, the collected powders were calcined at 500 °C for 2 h to obtain N–TiO_2. The fabrication of nanorods/graphene composites started with mixing under sonication for 30 min a specific amount of GO in 30 mL water/monoethanolamine solution ($V_{H_2O}/V_{EMA} = 1:1$). 1 mmol $Cd(OAc)_2$ and 1 mmol cysteine were then dissolved in the above mixture by stirring for 2 h. The product was transferred into a Teflon-lined autoclave and kept at 180 °C for 24 h.

2.5. Photocatalytic activity measurements

The photocatalytic activities of samples were evaluated by measuring the photodegradation of methyl orange (MO) under visible light. In a typical measurement, 20 mg photocatalysts were suspended in 20 mL of 25 ppm aqueous solution of MO. The solution was stirred in the dark for 2 h to achieve the equilibrium adsorption. Then the suspension was illuminated with a 500 W xenon lamp with a cutoff filter (λ > 400 nm). The concentration change of MO was monitored by measuring the UV–vis absorption of the suspensions at regular intervals. The suspension was centrifuged for 1 min to remove the photocatalysts before measurement. The peak absorbance of MO at 466 nm was used to determine its concentration. The photocatalytic activity was analyzed by the time profiles of C/C_0, where C is the concentration of MO at the irradiation time t and C_0 the concentration in the absorption equilibrium of the photocatalysts before irradiation, respectively. To investigate the photostability of as-prepared samples, photocatalysts was washed after each run and reused in the photodegradation of MO under visible light irradiation.

For the visible light photocatalytic reduction of Cr(VI), 10 mg pure In_2S_3 and In_2S_3 nanosheets/graphene composites were dispersed in 20 ml Cr(VI) solutions (10 mg/l), which were prepared by dissolving $K_2Cr_2O_7$ into deionized water. The mixed suspensions were magnetically stirred in the dark for 2 h to reach the adsorption–desorption equilibrium. Then the suspension was illuminated with a 500 W xenon lamp with a cutoff filter (λ > 420 nm). The normalized temporal concentration changes (C/C_0) of Cr(VI) are proportional to the normalized maximum absorbance (A/A_0), which can be derived from the change in the Cr(VI) absorption profile at a given time interval.

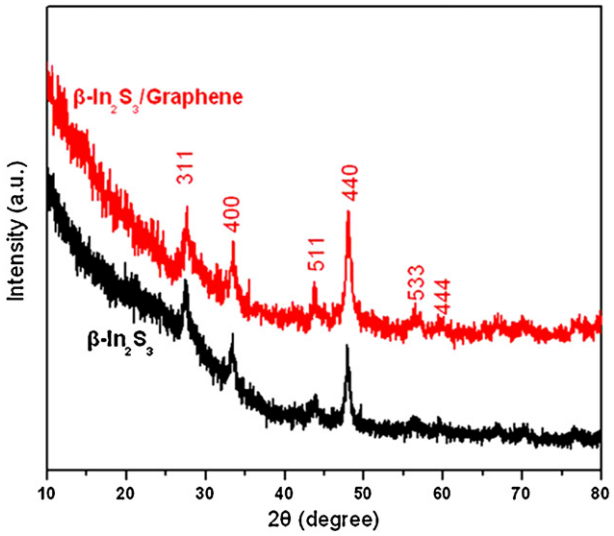

Fig. 1. XRD pattern of In_2S_3 and In_2S_3/graphene composites.

3. Results and discussion

Fig. 1 shows the XRD patterns of blank In_2S_3 and In_2S_3/1% graphene composites. It can be seen that both samples possess similar XRD patterns. All the diffraction peaks can be indexed to that of In_2S_3 with a cubic phase structure (JCPDS 32-0456). Compared to blank In_2S_3, no conventional stacking peak of graphene sheets is detected. As shown in Fig. S1, stacked graphene sheets are collected in the absence of In_2S_3, indicating that the in situ formation of In_2S_3 nanosheets on graphene prevents the restacking of the graphene layers.

Fig. 2a shows the morphology of pure In_2S_3 for the purpose of comparison. It is found that only irregular microparticles formed in the absence of GO. Fig. 2b is the TEM image of exfoliated GO, which is used as precursor to fabricate graphene-based composites. The obvious wrinkles and folds show clearly the 2-D structure of the transparent sheets. As can be seen in Fig. 2c,

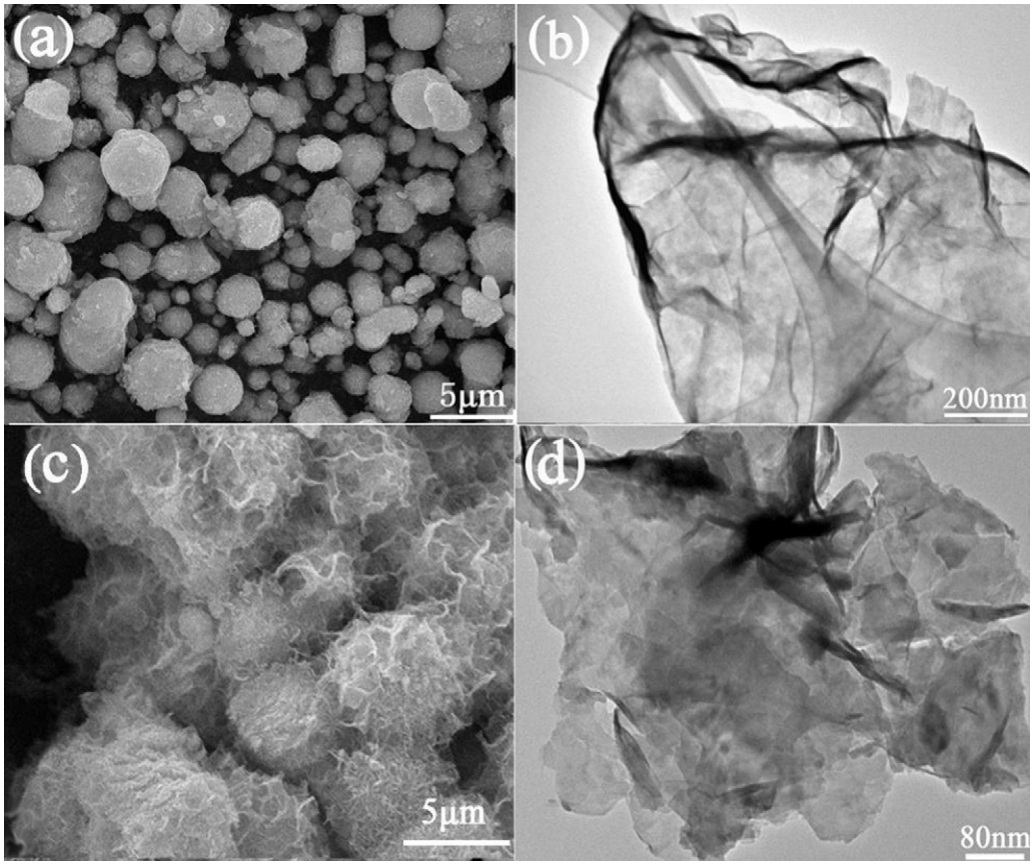

Fig. 2. (a) SEM image of blank In_2S_3; (b) TEM image of graphene oxide; (c) SEM image of In_2S_3/graphene composites; (d) TEM image of In_2S_3/graphene composites.

the as-synthesized In_2S_3/graphene composites show a typical 3-D sphere-like morphology. The self-assembled porous spheres are composed of several scaled and curved nanosheets, one piece of which is displayed in Fig. 2d. The overlap of several small nanosheets with larger substrate confirms the formation of In_2S_3 nanosheets/graphene nanocomposites.

To distinguish the graphene substrate from the curved nanosheets, HRTEM images are taken from the stretched and folded regions of the In_2S_3 nanosheets/graphene composites in Fig. 3a. Fig. 3b, shows the formation of an individual stretched In_2S_3 nanosheet with well-defined lattice fringes on the graphene substrate. The clear inter-planar distance is measured to be 3.24 Å, corresponding to the (3 1 1) plane of cubic In_2S_3. HRTEM image is collected from the exposed edge of In_2S_3 nanosheets. Fig. 3c shows the typical layered In_2S_3 with a few layers and an interlayer distance of 3.58 Å. These results suggest that In_2S_3 nanosheets have been intimately oriented on the graphene support. EELS spectrum in the carbon K-edge region is used to investigate the bonding configuration of graphene substrate in the composites. In Fig. 3d, the distinct $1s \rightarrow \pi^*$ (285 eV) and $1s \rightarrow \sigma^*$ (292 eV) peaks of the C K-edge are characteristic of sp^2-hybridized carbon network, indicating the existence of graphene in the composites [14].

XPS was employed to study the chemical states of In_2S_3 nanosheets/graphene composites. In Fig. 4a, the four peaks located at 284.8, 286.9, 287.9 and 289.1 eV can be assigned to the C—C, C—O, C=O and O—C=O bonds, respectively [15]. The content of C—C/C=C groups in the composites is calculated to be about 94.3%. As reported in our previous paper, the content of C—C/C=C groups in graphene oxide is only 41.9% [13]. The much higher content of C—C/C=C groups indicates that significant sp^3/sp^2-hybridized carbon structures are restored after the hydrothermal reduction. In Fig. 4b, the Raman spectrum of graphene oxide reveals both characteristic G and D bands around 1600 cm^{-1} and 1356 cm^{-1}. However, the G peak of the In_2S_3/graphene composites shifts in a low-wavelength direction. The intensity ratio of the G to D band (I_G/I_D) is a measure of the degree of graphitization. A significant increase in the I_G/I_D ratio is observed in the spectrum of In_2S_3/graphene composites. These results confirm deoxygenation of graphene oxide and the re-established conjugated graphene network [16]. We carried out the UV/vis absorption studies to investigate the optical property of the In_2S_3 nanosheets/graphene composites. As shown in Fig. 4c, as-synthesized product shows the step-like contours, with strong absorption all over the visible light range and significant ascension around 400 nm. These characteristics should be attributed to the valence-to-conduction band transition in In_2S_3. The E_g value of In_2S_3 is calculated to be 2.9 eV from the linear approximation of $(\alpha h\nu)^2$ vs. $h\nu$ plot, which is larger than that of bulk In_2S_3 (2.0–2.3 eV) [17]. As the excitonic radius of In_2S_3 is reported to be 33.8 nm, the blue-shifted band edge observed is the indication of quantum confinement effect resulting from their relatively small size [18,19]. It is expected to substantially alter the optoelectronic property of materials and enhance the utilization of solar energy in photocatalysis. The photoelectrochemical behaviour of the pure In_2S_3 and In_2S_3/graphene composites with a cutoff filter is shown in Fig. 4d. Obviously, the photocurrent of In_2S_3/graphene composites to each switch-on and switch-off event is increased drastically. It is known that the photocurrent is formed mainly by the diffusion of the photogenerated electrons to the back contact. Therefore, the enhanced photocurrent indicates a more efficient separation of the photoexcited electron–hole pairs as compared with pure In_2S_3[20].

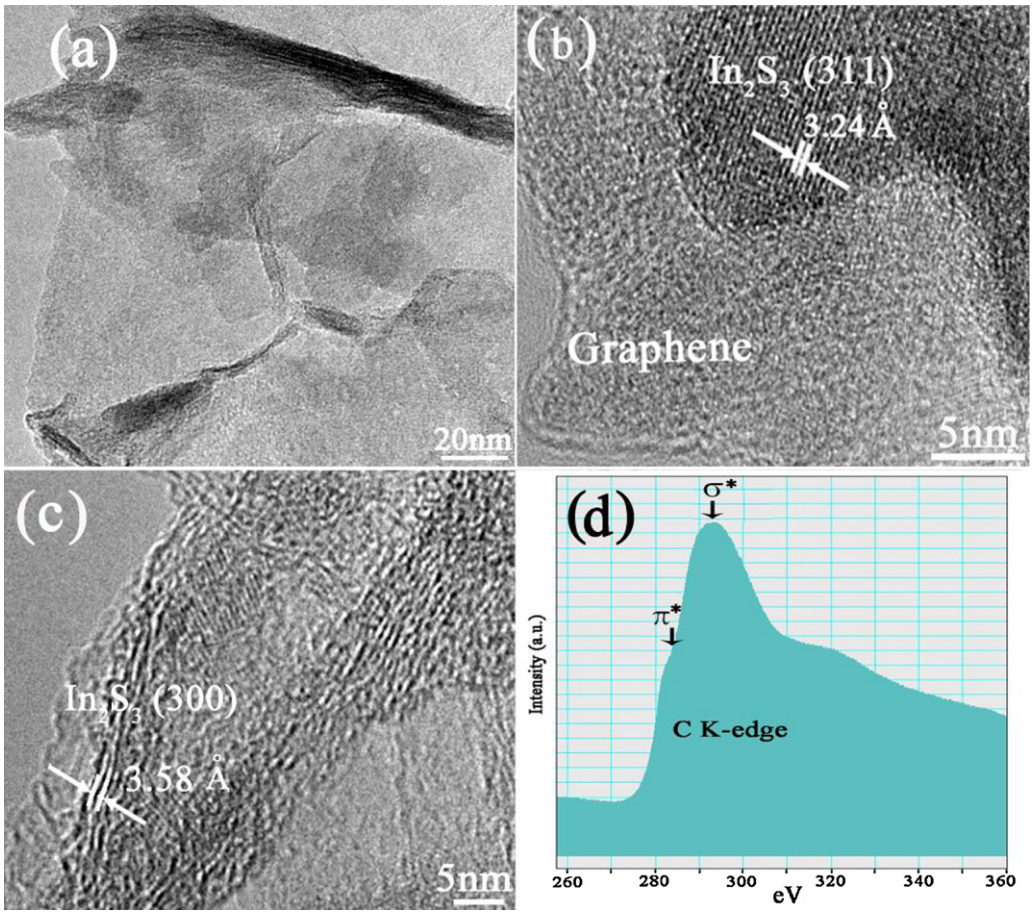

Fig. 3. (a–c) TEM and HRTEM images of In_2S_3 nanosheets/graphene composites; (d) typical EEL core loss K-edges of C at graphene substrate in the composites.

As illuminated in Scheme 1, the functional groups in cysteine molecule are crucial for the self-assembled growth of In_2S_3 nanosheets/graphene composites, such as —NH_2, —COOH, and —SH. At the initial stage I, a complex is formed via the coordination between In^{3+} ions and —SH of cysteine because of their strong interactions [21]. Then the complex is self-assembled anchored on the surface of graphene oxide at stage II, possibly through the abundant functional groups of cysteine (carboxyl, amino) and graphene oxide sheets (hydroxyl, carboxyl and epoxy groups). During the hydrothermal process in Stage III, the broken of S—C bonds results in the formation of In_2S_3 nuclei [7,22]. Here, cysteine acts as a sulfide source and grafting molecular, facilitating the in situ incorporation of In_2S_3 nanosheets with supports. Furthermore, the reduction of graphene oxide to graphene is reasonable expected because of the release of H_2S with appropriate reducing ability [23]. Accompanied with the growth of In_2S_3 nanosheets and the simultaneous reduction of graphene, In_2S_3 nanosheets/graphene composites begin to form. The partial overlap or coalescence of graphene sheets finally results in the formation of 3-D cross-linked architecture (Stage IV).

MO is a very stable azo dye and is usually taken as a model pollutant to evaluate the photocatalytic activity of photocatalysts under visible light irradiation. As shown in Fig. 5a, no obvious change in the concentration of MO is seen, without the addition of photocatalysts. The apparent rate constant for the photodecomposition of MO is calculated by the following equation: $k = \ln(C_0/C)/t$ [24]. In_2S_3 nanosheets/graphene composite with 1% graphene shows the highest average apparent rate ($k = 0.039\ min^{-1}$), which is more than 5 times higher than that of pure In_2S_3 ($k = 0.0067\ min^{-1}$). This suggests that the introduction of graphene can efficiently improve the photocatalytic activity of In_2S_3. Because of the "shielding effect", the larger percentage of graphene leads to the deterioration of the photocatalytic performance [12]. The reaction temperature and molar ratio of cysteine/In^{3+} show significant influence on the photocatalytic performance of products. As shown in Fig. 5b, In_2S_3 nanosheets/graphene composites fabricated at the temperature of 180 °C shows much higher activity than that of 150 °C and 200 °C. Besides, the cysteine/In^{3+} ratio of 3 is beneficial for the superior photocatalytic efficiency, as can be seen in Fig. 5c. To confirm the advantage of the cysteine-assisted method, In_2S_3/graphene composites are also prepared using thiourea and thioacetamide as sulfide sources. As shown in Fig. 5d, In_2S_3 nanosheets/graphene composites also show the highest efficiency for the degradation of MO, when cysteine is used as raw materials.

To further illustrate the strong photocatalytic ability of In_2S_3/graphene composites, the decomposition of MO over several other common photocatalysts with high visible-light efficiency is also studied [25–27]. As shown in Fig. 6a–c, the reference photocatalysts include Ag_3PO_4,CdS nanorods/graphene composites and nitrogen doped TiO_2 (N–TiO_2). It is found that the photocatalytic degradation efficiency of MO follows the order In_2S_3 nanosheets/graphene > Ag_3PO_4 > CdS nanorods/graphene > N–TiO_2. The much superior activity of In_2S_3 nanosheets/graphene composites indicates their promising application for high-efficiency environmental remediation. Thus, the facile cysteine-assisted hydrothermal method shows significant advantage in the fabrication of metal sulfide/graphene photocatalysts.

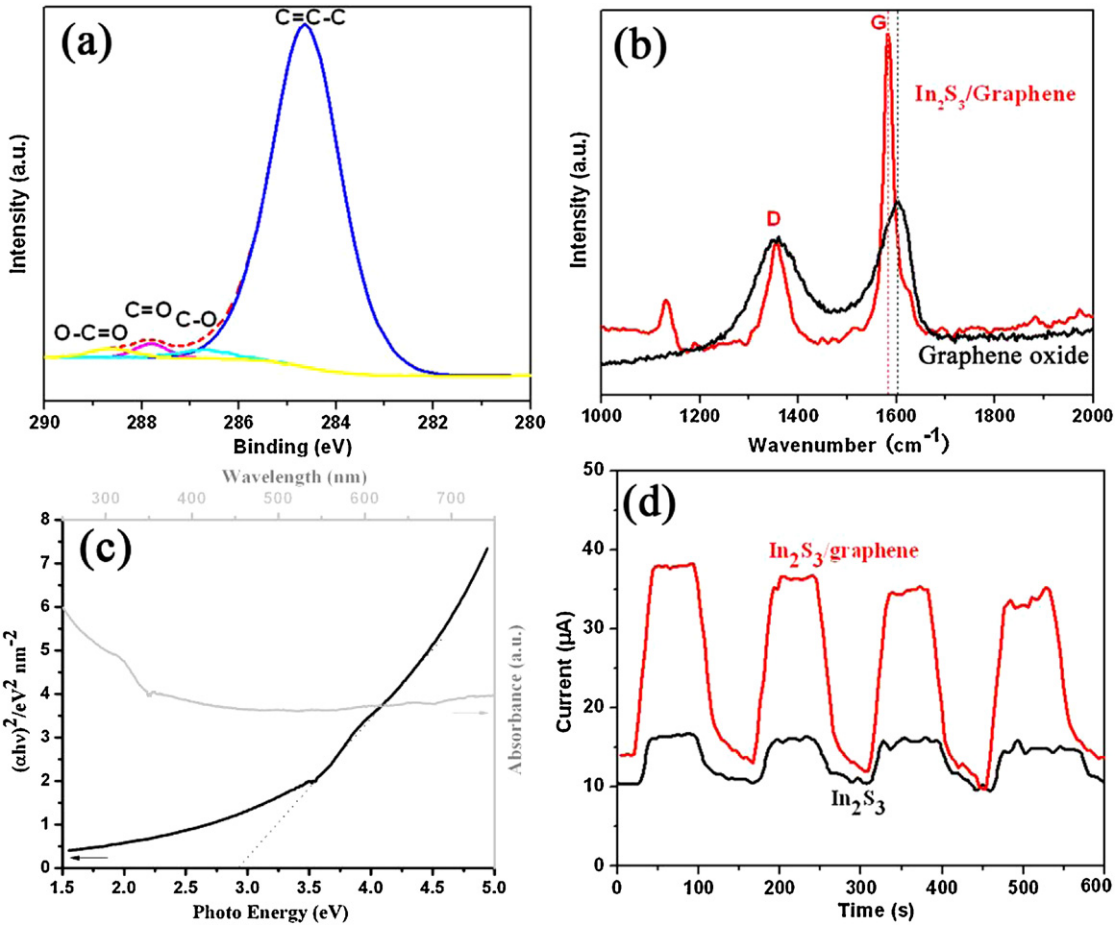

Fig. 4. (a) The C (1s) XPS core level of In_2S_3/graphene composites; (b) Raman spectra of graphene oxide and In_2S_3/graphene composites; (c) UV–vis spectra of In_2S_3/graphene composites and the corresponding plot of $(\alpha h\nu)^2$ vs. $h\nu$; (d) transient photocurrent response of In_2S_3 and In_2S_3/graphene composites under the irradiation of visible light.

Generally, the increased adsorptivity of pollutants, the enhanced light absorption and the efficient charge separation and transfer are crucial for the improved photocatalytic activity of photocatalysts. As reported, the hybridization of graphene can undoubtedly improve the dye adsoptivity and light absorption of semiconductor photocatalysts [28]. Besides these, the cysteine-assisted in situ reaction and the improved charge separation and transfer path are considered as the dominating reasons for the significantly enhanced photocatalytic performance of composites [29]. Firstly, the dual role of cysteine as reducing agent and sulfide donor facilitates the in situ formation of In_2S_3 nuclei on the substrate and the deoxygenation of graphene oxide during the growth of In_2S_3[30,31]. As a result, In_2S_3 nanosheets/graphene composites show perfect interfacial contact, which benefits the interfacial charge migration to electron acceptor. Furthermore, considering the work function of graphene (−4.42 eV) and the conduction band of In_2S_3, the direct transfer of electrons from the conduction band of In_2S_3 to graphene is favorable. Therefore, recombination of electrons with holes is significantly suppressed in the graphene-based photocatalytic composites [32,33].

Different pathways have been reported for the visible-light-driven photodegradation of MO, which can be discriminated by the active species operated on [34,35]. Thus, the additional conditions that influenced the generation of active species are imposed on the photodegradation process. As shown in Fig. S6, the roles of hydroxyl radicals, holes and O_2 in the photocatalytic reactions are

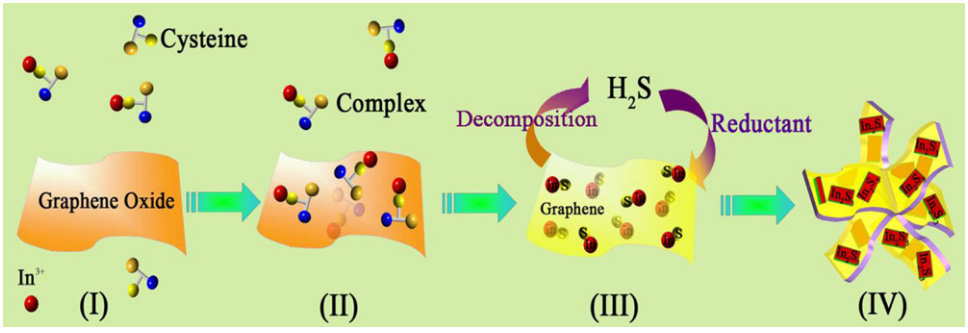

Scheme 1. Schematic diagram of the synthetic route for In_2S_3 nanosheets/graphene composites.

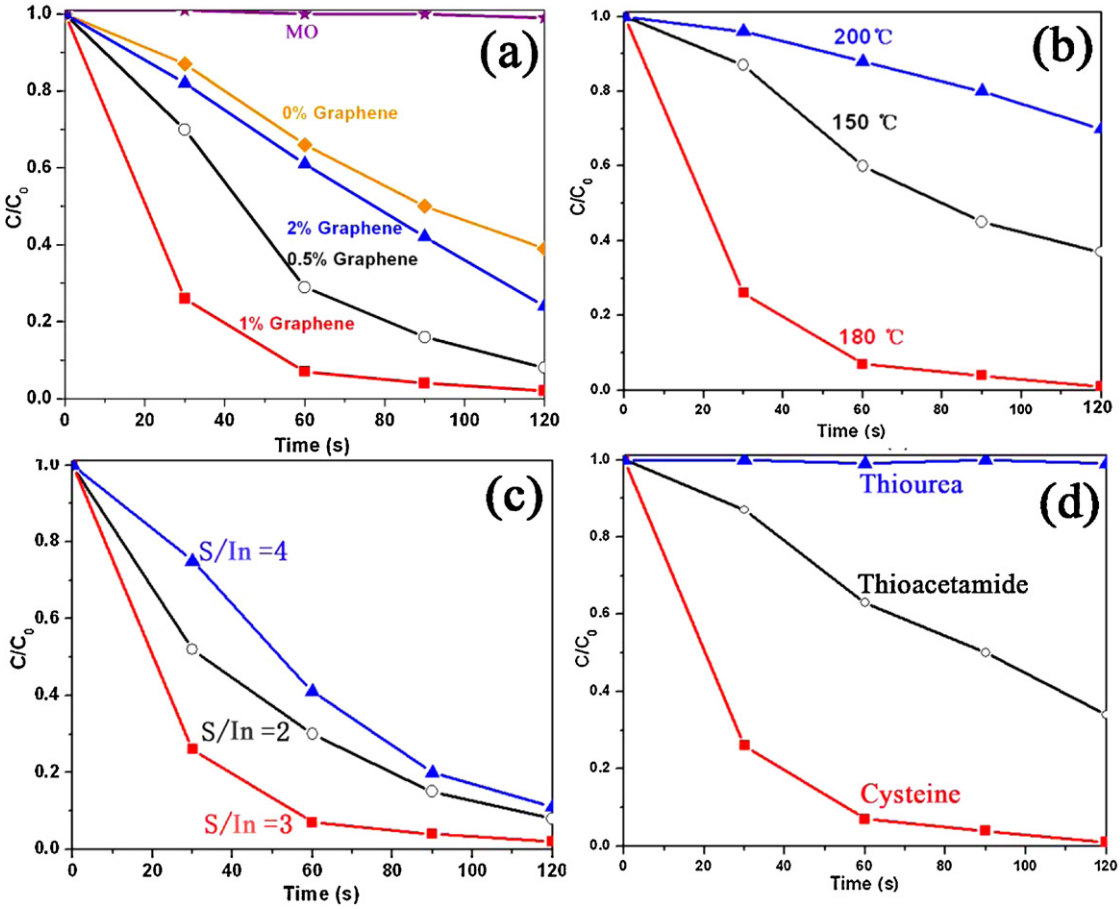

Fig. 5. Visible-light-driven photodegradation of MO over (a) In_2S_3/graphene composites with different amount of graphene; (b) In_2S_3/graphene composites fabricated under different temperature; (c) In_2S_3/graphene composites fabricated with different molar ratio of cysteine/In^{3+}; (d) In_2S_3/graphene composites fabricated from different sulfide donors.

investigated [36]. According to the effect of scavengers, the decomposition of MO molecules is attributed to the predominant action of oxidation action of the generated $^{\bullet}O_2^-$ radicals and subordinate hole oxidation process. Hydroxyl radical is confirmed to be insignificant for the decomposition of MO [37]. This is because that the valance band of In_2S_3 is more negative than E($^{\bullet}OH/OH^-$) (2.38 V vs. NHE) and E($^{\bullet}OH/H_2O$) (2.27 V vs. NHE), the photo-induced holes cannot oxidize OH^- and H_2O to produce hydroxyl radicals, but can oxidize dye molecules into final products directly [38].

Based on the above discussion, a possible mechanism for the photodegradation of MO under visible light is proposed in Scheme 2. Firstly, dye molecules adsorbed on composites are stimulated to the excited state under visible light irradiation [39]. Subsequently, the photoexcited dye injects electrons into the conduction band of In_2S_3 through the photosensitization process (Path I) [40]. Secondly, the role of graphene as electron acceptor leads to the charge transfer either from the excited dye molecules or the conduction band of In_2S_3 (path II and path III in Scheme 2). As reported, the existence of graphene with superior conductivity can significantly enhance the charge separation, which is crucial for the electron triggered photocatalytic reaction [41]. Thirdly, the electrons can be scavenged by molecular oxygen, resulting in the formation of abundant superoxide anion radicals. Herein, the $^{\bullet}O_2^-$ radicals are suggested as the dominant active species that can oxidize the adsorbed pollutants [42]. Finally, the dye molecules are also oxidized by the photo-generated holes in the valance band of In_2S_3 (path IV in Scheme 2) [43].

The stability of In_2S_3 nanosheets/graphene composites was evaluated. Fig. 7 clearly shows that no noticeable deactivation occurs in the repeat uses, indicating a high photostability of In_2S_3 nanosheets/graphene composites. The improved photostability is also due to the high-efficiency separation of electron–hole pairs in the presence of graphene [44]. Hexavalent chromium is of particular environmental concern due to its toxicity and mobility and is difficult to remove from industrial wastewater [45]. Cr(VI) usually presents in the form of highly soluble, toxic and carcinogenic chromate anions. It can be converted into Cr(III), which exhibits lower toxicity and mobility in the environment, by photocatalytic reduction on semiconductors [46]. The ability of In_2S_3 nanosheets/graphene composites for photocatalytic reduction of Cr(VI) has also been evaluated in this study. As shown in Fig. 8a, the removal rate of Cr(VI) for pure In_2S_3 and In_2S_3 nanosheets/graphene composites are 58% and 78% in 12 min. These values reach 88% and 95% after 20 min. The superior activity of the composites confirms that the introduction of graphene can significantly improve the visible-light activity of In_2S_3.

In Fig. 8b, a possible mechanism is proposed to illustrate the superior photoreduction performance of In_2S_3 nanosheets/graphene composites [47]. During the photocatalytic reduction of Cr(VI), In_2S_3 nanomaterials is excited by the absorption of photons and electron–hole pairs are created. The photogenerated electrons can reduce $Cr_2O_7^{2-}$ to Cr^{3+}, according to the reduction reaction as Eq. (1). Meanwhile, the photo-generated holes show much stronger oxidation ability. This is because of the

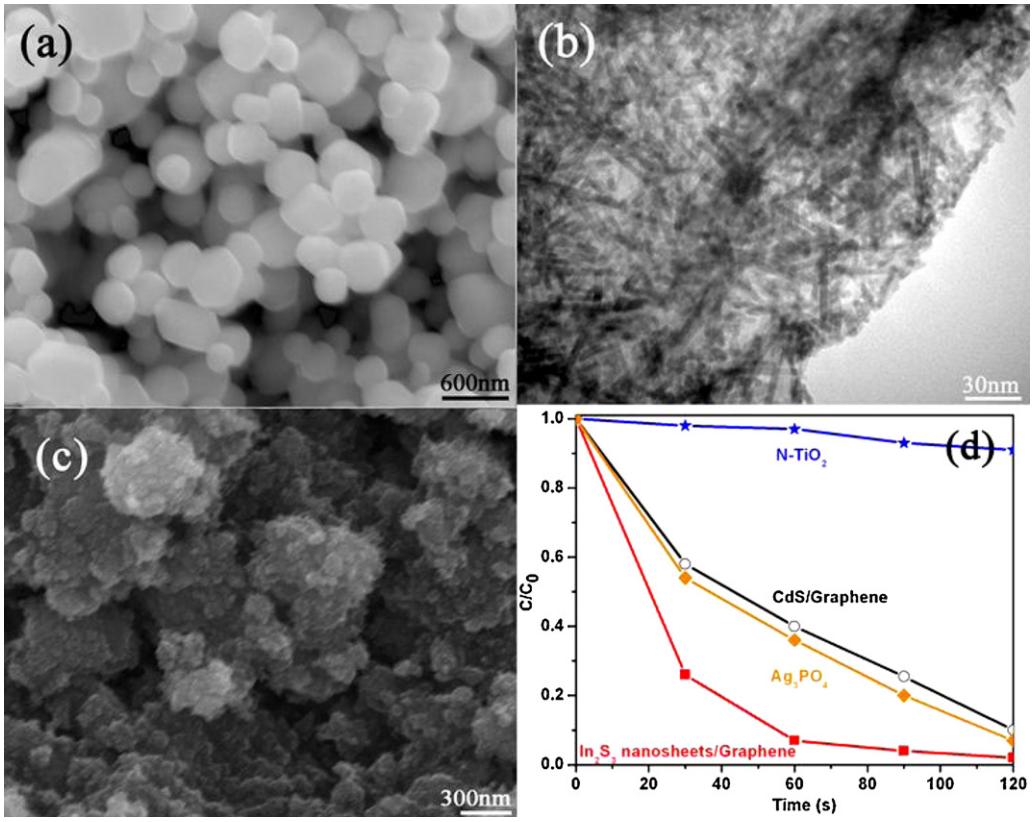

Fig. 6. SEM images of reference photocatalysts: (a) Ag_3PO_4; (b) CdS nanorods/graphene composites; (c) N–TiO_2. (d) Visible-light-driven photodegradation of MO over various semiconductor photocatalysts.

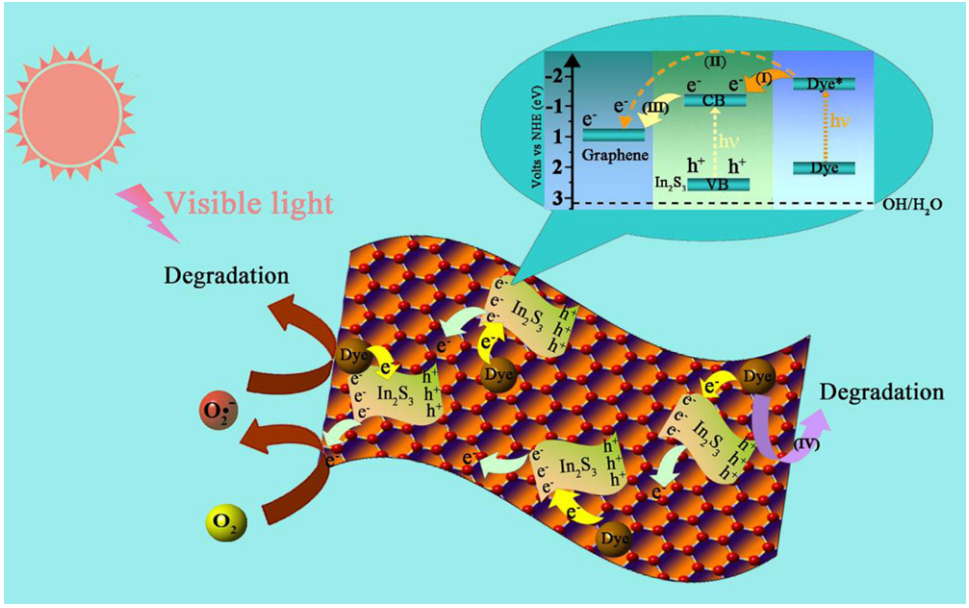

Scheme 2. Schematic illustration showing the reaction mechanism for photocatalytic degradation.

widened band gap resulted from the quantum confinement effect. Since the valence band of In_2S_3 is more negative than the oxidation potential of water (1.23 V vs. NHE) [48], water molecules can be oxidized by the holes as shown in Eq. (2). Similar results have been reported in the literature for photocatalytic water splitting involving In_2S_3 nanosheets [49].

$$Cr_2O_7^{2-} + 14H^+ + 6e^- \rightarrow 2Cr^{3+} + 7H_2O \quad (1)$$

$$2H_2O + 4h^+ \rightarrow O_2 + 4H^+ \quad (2)$$

As for In_2S_3 nanosheets/graphene composites, the superior conductivity of graphene facilitates the transfer of photo-induced electrons from the conduction band of In_2S_3 to graphene. It is believed that the role of graphene as electron mediator can significantly inhibit the recombination of charge carriers in In_2S_3, which offers more active sites for the reduction of Cr(VI) [50].

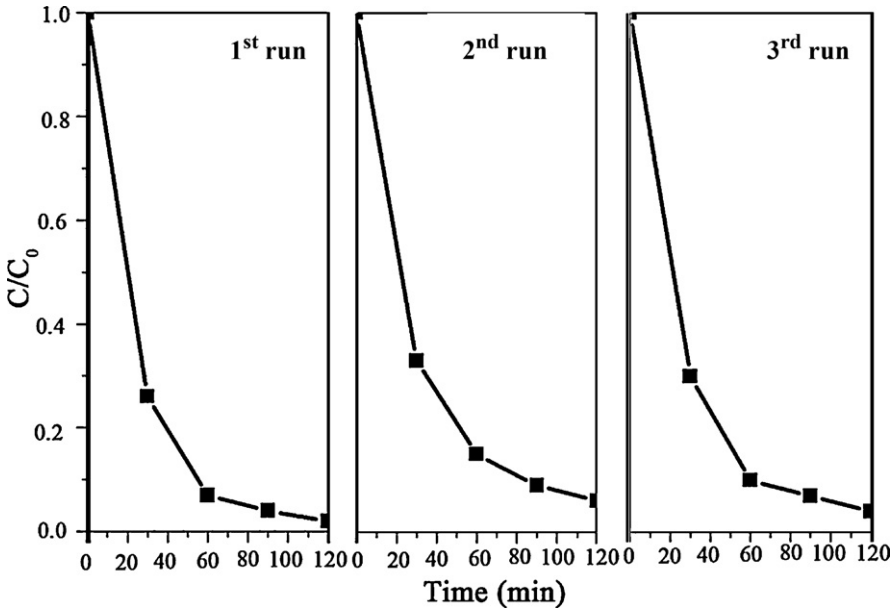

Fig. 7. Recycled photodegradation of MO under the irradiation of visible light over In_2S_3 nanosheets/graphene composites.

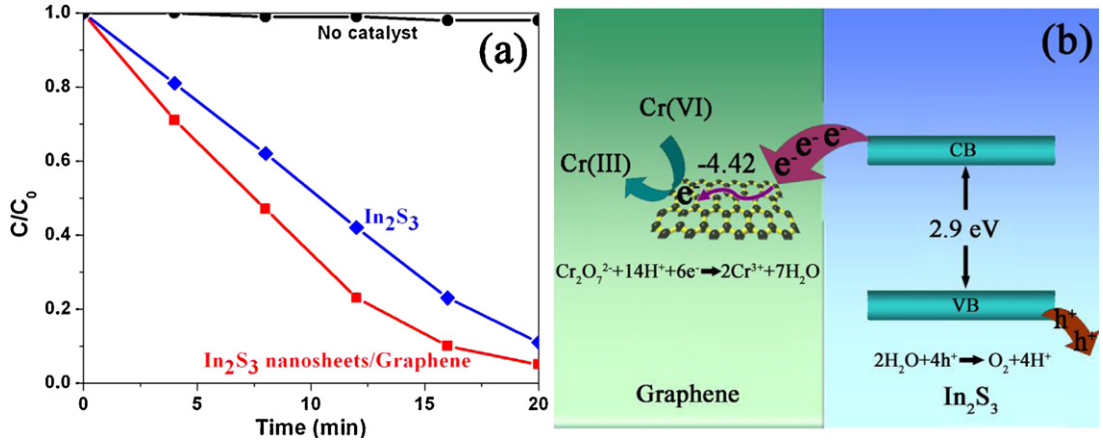

Fig. 8. (a) Photocatalytic reduction of Cr(VI) over In_2S_3 and In_2S_3 nanosheets/graphene composites; (b) schematic diagram of energy levels of In_2S_3 and graphene.

4. Conclusion

In summary, we have demonstrated an effective method to prepare In_2S_3 nanosheets/graphene photocatalysts, employing cysteine as a complexing agent, sulfide source and reducing agent. The incorporation of graphene preserves its high conductivity and greatly enhances the photocatalytic activity of the products. In_2S_3 nanosheets/graphene composites show superior activity than the reference visible-light-driven photocatalysts and In_2S_3/graphene composites fabricated from different sulfide sources. The excellent photocatalytic performance of the In_2S_3 nanosheets/graphene composite is attributed to the perfect interfacial contact between the two components and the fast interfacial charge transfer from In_2S_3 nanosheets to graphene. Overall, this work provides a new option for the fabrication of high-efficiency photocatalysts for environmental remediation and energy conversion.

Acknowledgments

This work was supported by the Focused Investments Scheme of The Chinese University of Hong Kong, the Research Grants Council of the Hong Kong Special Administration Region, China (Project 404810), the National Natural Science Foundation of China (21173179) and the Natural Science Foundation of Hebei Province (E2010001932).

Appendix A. Supplementary data

Supplementary data associated with this article can be found, in the online version, at http://dx.doi.org/10.1016/j.apcatb.2012.09.008.

References

[1] A. Kubacka, M. Fandez-García, G. Colon, Chemical Reviews 112 (2012) 1555–1614.
[2] H. Tong, S. Ouyang, Y. Bi, N. Umezawa, M. Oshikiri, J. Ye, Advanced Materials 24 (2011) 229–251.
[3] M.D. Hernandez-Alonso, F. Fresno, S. Suarez, J.M. Coronado, Energy & Environmental Science 2 (2009) 1231–1257.
[4] Y. Bi, S. Ouyang, N. Umezawa, J. Cao, J. Ye, Journal of the American Chemical Society 133 (2011) 6490–6492.
[5] H. Yu, R. Liu, X. Wang, P. Wang, J. Yu, Applied Catalysis B 111–112 (2012) 326–333.
[6] A. Cao, Z. Liu, S. Chu, M. Wu, Z. Ye, Z. Cai, Y. Chang, S. Wang, Q. Gong, Y. Liu, Advanced Materials 22 (2010) 103–106.

[7] S. Rengaraj, S. Venkataraj, C. Tai, Y. Kim, E. Repo, M. Sillanpaa, Langmuir 27 (2011) 5534–5541.
[8] K.H. Park, K. Jang, S.U. Son, Angewandte Chemie International Edition 45 (2006) 4608–4612.
[9] Y.H. Kim, J.H. Lee, D. Shin, S.M. Park, J.S. Moon, J.G. Nam, J. Yoo, Chemical Communications 46 (2010) 2292–2294.
[10] M.A. Franzman, R.L. Brutchey, Chemistry of Materials 21 (2009) 1790–1792.
[11] X. An, J.C. Yu, RSC Advances 1 (2011) 1426–1434.
[12] Q. Li, B. Guo, J. Yu, J. Ran, B. Zhang, H. Yan, J.R. Gong, Journal of the American Chemical Society 33 (2011) 10878–10884.
[13] X. An, J.C. Yu, Y. Wang, Y. Hu, X. Yu, G. Zhang, Journal of Materials Chemistry 22 (2012) 8525–8531.
[14] Y. Zhu, S. Murali, M. Stoller, K. Ganesh, W. Cai, P. Ferreira, A. Pirkle, R. Wallace, K. Cychosz, M. Thommes, D. Su, E. Stach, R. Ruoff, Science 332 (2011) 1537–1541.
[15] O. Akhavan, ACS Nano 4 (2010) 4174–4180.
[16] C. Wu, Y. Zhang, S. Li, H. Zheng, H. Wang, J. Liu, K. Li, H. Yan, Journal of Chemical Engineering 178 (2011) 468–474.
[17] L. Zhang, W. Zhang, H. Yang, W. Fu, W. Zhao, H. Zhao, J. Ma, Materials Chemistry and Physics 130 (2011) 932–936.
[18] M. Franzman, R. Brutchey, Chemistry of Materials 21 (2009) 1790–1792.
[19] B.G. Kumar, K. Muralidharan, Journal of Materials Chemistry 21 (2011) 11271–11275.
[20] N. Zhang, Y. Zhang, X. Pan, X. Fu, S. Liu, Y. Xu, Journal of Physical Chemistry C 115 (2011) 23501–23511.
[21] W. Qiu, M. Xu, X. Yang, F. Chen, Y. Nan, J. Zhang, H. Iwaic, H. Chen, Journal of Materials Chemistry 21 (2011) 13327–13333.
[22] P. Zhao, T. Huang, K. Huang, Journal of Physical Chemistry C 111 (2007) 12890–12897.
[23] K. Chang, W. Chen, ACS Nano 5 (2011) 4720–4728.
[24] Y. Liang, H. Wang, H. Casalongue, Z. Chen, H. Dai, Nano Research 3 (2010) 701–705.
[25] Z. Yi, J. Ye, N. Kikugawa, T. Kako, S. Ouyang, H. Stuart-Williams, H. Yang, J. Cao, W. Luo, Z. Li, Y. Liu, R.L. Withers, Nature Materials 9 (2010) 559–564.
[26] K. Wu, H. Zhu, Z. Liu, W. Rodríguez-Córdoba, T. Lian, Journal of the American Chemical Society 134 (2012) 10337–10340.
[27] K. Wu, H. Zhu, Z. Liu, W. Rodriguez-Cordoba, T. Lian, Journal of the American Chemical Society 25 (2012) 10337–10340.
[28] Y. Zhang, Z. Tang, X. Fu, Y. Xu, ACS Nano 4 (2010) 7303–7314.
[29] K. Chang, Z. Wang, G. Huang, H. Li, W. Chen, J. Lee, Journal of Power Sources 201 (2012) 259–266.
[30] D. Chen, L. Li, L. Guo, Nanotechnology 22 (2011) 325601.
[31] Y.T. Liang, B.K. Vijayan, K.A. Gray, M.C. Hersam, Nano Letters 11 (2011) 2865–2870.
[32] C. Chen, W. Cai, M. Long, B. Zhou, Y. Wu, D. Wu, Y. Feng, ACS Nano 4 (2010) 6425–6432.
[33] Q. Xiang, J. Yu, M. Jaroniec, Chemical Society Reviews 41 (2012) 782–796.
[34] W. Li, D. Li, Y. Lin, P. Wang, W. Chen, X. Fu, Y. Shao, Journal of Physical Chemistry C 116 (2012) 3552–3560.
[35] X. Lin, F. Huang, W. Wang, Y. Wang, Y. Xia, J. Shi, Applied Catalysis A: General 313 (2006) 218–223.
[36] L. Zhao, X. Chen, X. Wang, Y. Zhang, W. Wei, Y. Sun, M. Antonietti, M. Titirici, Advanced Materials 22 (2010) 3317–3321.
[37] Y. Li, J. Wang, H. Yao, L. Dang, Z. Li, Journal of Molecular Catalysis A: Chemical 334 (2011) 116–122.
[38] H. Cheng, B. Huang, Y. Dai, X. Qin, X. Zhang, Langmuir 26 (2010) 6618–6624.
[39] W. Li, D. Li, S. Meng, W. Chen, X. Fu, Y. Shao, Environmental Science and Technology 45 (2011) 2987–2993.
[40] J. Jiang, K. Zhao, X. Xiao, L. Zhang, Journal of the American Chemical Society 134 (2012) 4473–4476.
[41] I. Lightcap, T. Kosel, P. Kamat, Nano Letters 10 (2010) 577–583.
[42] J. Zhuang, Q. Tian, H. Zhou, Q. Liu, P. Liu, H. Zhong, Journal of Materials Chemistry 22 (2012) 7036–7042.
[43] J. Shi, X. Yan, H. Cui, X. Zong, M. Fu, S. Chen, L. Wang, Journal of Molecular Catalysis A: Chemical 356 (2012) 53–60.
[44] L. Jia, D. Wang, Y. Huang, A. Xu, H. Yu, Journal of Physical Chemistry C 115 (2011) 11466–11473.
[45] H. Ma, J. Shen, M. Shi, X. Lu, Z. Li, Y. Long, N. Li, M. Ye, Applied Catalysis B: Environmental 121–122 (2012) 198–205.
[46] H. Ma, Y. Zhang, Q. Hu, D. Yan, Z. Yu, M. Zhai, Journal of Materials Chemistry 22 (2012) 5914–5916.
[47] X. Liu, L. Pan, T. Lv, T. Lu, G. Zhu, Z. Sun, C. Sun, Catalysis Science & Technology 1 (2011) 1189–1193.
[48] F. Osterloh, Chemistry of Materials 20 (2008) 35–54.
[49] X. Fu, X. Wang, Z. Chen, Z. Zhang, Z. Li, D. Leung, L. Wu, X. Fu, Applied Catalysis B: Environmental 95 (2010) 393–399.
[50] X. Liu, L. Pan, T. Lv, G. Zhu, Z. Sun, C. Sun, Chemical Communications 47 (2011) 11984–11986.